Impedance Reshaping Method of DFIG System Based on Compensating Rotor Current Dynamic to Eliminate PLL Influence

Xiaoling Xiong, *Member, IEEE*, Bochen Luo, Longcan Li, Ziming Sun, *Member, IEEE*, and Frede Blaabjerg, *Fellow, IEEE*

***Abstract*—The phase-locked loop (PLL) used in the doubly-fed induction generator (DFIG) can cause frequency-coupling phenomena, which will give negative-resistance characteristics of the DFIG at a low frequency, resulting in stability issues under weak-grid operation. Based on the multi-input multi-output impedance model of the DFIG system, it is found that the frequency-coupling phenomena are mainly introduced by the transfer function matrix related to the rotor current dynamic. This article presents an improved impedance reshaping method based on compensating the rotor current dynamic to reduce the influence of PLL, in which the rotor current dynamic is compensated before being introduced to the PI controller. Thus, the frequency-coupling effect can be almost eliminated, and the stability of the DFIG is improved a lot. Furthermore, a simplified compensation method is proposed, which can easily be implemented. The robustness analysis is performed to illustrate the availability of the proposed methods when the system operating conditions and parameters vary. Finally, control-hardware-in-the-loop experiments are also carried out, and the results validate the effectiveness of the proposed methods.**

***Index Terms*—Doubly-fed induction generator (DFIG), frequency-coupling phenomena, impedance reshaping, phase-locked loop (PLL), small-signal stability.**

I. Introduction

WIND power generation based on doubly-fed induction generator (DFIG) systems has been developing rapidly [1], [2]. However, with the increasing penetration of renewable energy, the ac grid connected to them becomes weaker, giving the characteristic of a low short-circuit ratio (SCR) [3], [4], [5]. For the DFIG system, the classic control strategy uses a phase-locked loop (PLL) to synchronize with the grid, such as orienting the point of common coupling (PCC) voltage to facilitate vector control [6], [7]. However, the asymmetric control structure of the PLL causes the frequency-coupling phenomena, which may aggravate the negative-resistance characteristics of the DFIG system at low frequencies, reducing the stability margin of the interconnected system [8], [9].

To solve the stability issue caused by PLL, many different methods have been proposed. One basic idea is to modify or enhance the vector control by using an extra controller. For example, a damping controller [10], [11] or a virtual impedance controller [12], [13] is proposed to suppress sub/supersynchronous oscillations in DFIG. However, the effectiveness can easily be influenced by operating conditions or system parameters. To improve the adaptability of the control system, adaptive control strategies are further proposed in [14], which can suppress the oscillation of the DFIG system under different operating conditions, however, making the control structure more complex.

Other research efforts have been devoted to finding new control strategies for DFIG to replace conventional vector control based on PLL. The authors in [15] and [16] adopt direct power control (DPC) to eliminate the influence of PLL by introducing a virtual *d-q* frame rotating at a constant speed to replace the synchronous rotating *d-q* frame. However, strong frequency-coupling characteristics at high frequencies are introduced by the DPC, leading to high-frequency stability issues.

In [17], a symmetrical PLL is proposed, which is able to introduce the dynamics of PLL to the *d-q* axis symmetrically, making the whole system become a single-input and single-output (SISO) system. Although the symmetrical PLL can eliminate frequency-coupling phenomena and facilitate stability analysis, it does not fundamentally remove the negative resistance introduced by the PLL. In [18], symmetrical PLL is applied to the DFIG system to eliminate the off-diagonal elements of the impedance matrix. However, the symmetrical PLL can simplify the DFIG impedance model only when other control loops are symmetrical too. Supposing the asymmetric control loops, such as the dc-link voltage loop on the grid-side converter (GSC), are considered. In that case, frequency-coupling phenomena will still exist even if the symmetrical PLL is adopted. In [19], an impedance reshaping method based on virtual impedance is further proposed to enhance the stability of the DFIG system with symmetrical PLL.

Manuscript received 16 August 2023; revised 2 November 2023; accepted 16 December 2023. Date of publication 22 December 2023; date of current version 16 February 2024. This work was supported in part by the National Key Research and Development Program of China under Grant 2021YFB2601602 and in part by the Fundamental Research Funds for the Central Universities under Grant 2022MS004. Recommended for publication by Associate Editor J. Ye. *(Corresponding author: Xiaoling Xiong.)*

Xiaoling Xiong, Bochen Luo, Longcan Li, and Ziming Sun are with the School of Electrical and Electronic Engineering, North China Electric Power University, Beijing 102206, China (e-mail: xiongxl1102@ncepu.edu.cn; luobochen2021@ncepu.edu.cn; longcanlee@126.com; ktyope@sina.com).

Frede Blaabjerg is with the Department of Energy, Aalborg University, 9220 Aalborg, Denmark (e-mail: fbl@et.aau.dk).

Color versions of one or more figures in this article are available at https://doi.org/10.1109/TPEL.2023.3346042.

Digital Object Identifier 10.1109/TPEL.2023.3346042

This article is going to put forward a general impedance reshaping method based on eliminating the dynamics of rotor current to reduce the frequency-coupling phenomena of the DFIG system caused by PLL, thus improving the stability of the interconnected system. The contributions of this article can be summarized as follows.

1) Based on the multi-input multi-output (MIMO) impedance model of the DFIG system, the impact of PLL is analyzed, and their contributions to the relative transfer function matrices are revealed. It is found that the frequency-coupling phenomena are mainly caused by the transfer function matrix linked to the rotor current dynamic.
2) To eliminate the rotor current dynamic introduced by PLL, a second-order impedance reshaping method based on compensating the rotor current dynamic is proposed, which can not only eliminate the frequency-coupling phenomena caused by the PLL but also remove the negative-resistance region and improve the stability margin of the DFIG system.
3) A first-order reshaping method is further obtained based on simplifying the second-order impedance reshaping method, which can also effectively suppress the oscillations.
4) Robustness analysis is carried out, illustrating that both the proposed methods can reduce the negative-resistance region and improve the stability margin of the system when the operating conditions and parameters vary.

To present all the issues, the rest of the article is organized as follows. Section II gives the DFIG system configuration, and the corresponding impedance model is presented. The contributions of different PLL-related matrices to frequency-coupling phenomena are revealed. In Section III, the second-order impedance reshaping method based on compensating the rotor current dynamic is proposed, and the simplified first-order method is further deduced. Section IV gives the robustness analysis to verify the effectiveness of the proposed methods when the system operating conditions and parameters vary. Section V shows the experimental results to verify the theoretical analysis. Finally, Section VI concludes this article.

II. Impedance Model of DFIG System

A. DFIG System Configuration

DFIG system is mainly composed of DFIG, rotor-side converter (RSC), and GSC. The main task of DFIG+RSC is to realize maximum power point tracking and control the output power at the stator side while the GSC is employed to stabilize the common dc-link voltage. Considering that the dc voltage is controlled to be constant by the outer-loop regulator of the GSC, the DFIG+RSC and GSC can be modeled separately, which are further paralleled to obtain the impedance model of the overall DFIG system. As the power exchange is mainly achieved by DFIG+RSC and the inductance of the filter on the GSC side is large, the amplitude of the GSC impedance will be much greater than that of DFIG+RSC. Thus, the GSC has less influence on the impedance of the DFIG system, which even can be ignored further [18]. In this article, only the impedance of DFIG+RSC is considered.

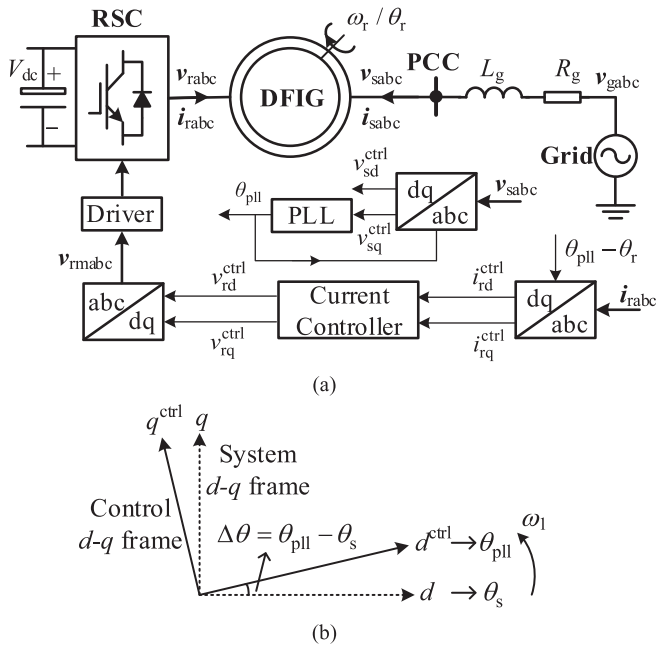

Fig. 1. Topology of the DFIG system and the relationship between different d-q frames. (a) Topology of the DFIG system connected to the ac grid. (b) Diagram of the system and control d-q frames.

The topology and control diagram of DFIG+RSC are shown in Fig. 1(a). $\boldsymbol{v}_{\mathrm{sabc}}$, $\boldsymbol{i}_{\mathrm{sabc}}$, $\boldsymbol{v}_{\mathrm{rabc}}$, and $\boldsymbol{i}_{\mathrm{rabc}}$ represent the voltage and current vectors at the stator and rotor side, respectively, and $\boldsymbol{v}_{\mathrm{gabc}}$ is the ac-grid voltage vector. The subscript abc denotes that they are in the three-phase stationary frame. The aforementioned vectors can also be expressed in a synchronous rotating frame (d-q), i.e., $\boldsymbol{v}_{\mathrm{sdq}}, \boldsymbol{i}_{\mathrm{sdq}}, \boldsymbol{v}_{\mathrm{rdq}}, \boldsymbol{i}_{\mathrm{rdq}}$, and $\boldsymbol{v}_{\mathrm{gdq}}$. For example, the stator voltage vector in the two frames can be expressed as $\boldsymbol{v}_{\mathrm{sabc}} = [v_{\mathrm{sa}}\ v_{\mathrm{sb}}\ v_{\mathrm{sc}}]^{\mathrm{T}}$ and $\boldsymbol{v}_{\mathrm{sdq}} = [v_{\mathrm{sd}}\ v_{\mathrm{sq}}]^{\mathrm{T}}$. R_{g} and L_{g} are the equivalent resistance and inductance of the grid, respectively. V_{dc} is the dc-link voltage, which can be regarded as a constant. The rotor angular frequency ω_{r} and rotor angle θ_{r} are obtained by an encoder. θ_{pll} is obtained by the PLL. Considering the perturbations of PCC voltage and the dynamics of PLL, there will be two different d-q frames, i.e., the system d-q frame and the control d-q frame [20]. Both d-q frames are rotating in the synchronous frequency, and their relationship is depicted in Fig. 1(b). θ_{s} is the real phase angle of the PCC voltage in the system d-q frame, and a phase error $\Delta\theta$ is introduced by the PLL dynamics when the PCC voltage varies. To distinguish from the components in the system d-q frame, the superscript ctrl is used to denote the components in the control d-q frame.

B. Impedance Model of DFIG in d-q Frame

The voltage and flux equations of the DFIG in the d-q frame can be expressed as follows:

$$\begin{cases} v_{\mathrm{sd}} = R_{\mathrm{s}} i_{\mathrm{sd}} + p\psi_{\mathrm{sd}} - \omega_1 \psi_{\mathrm{sq}} \\ v_{\mathrm{sq}} = R_{\mathrm{s}} i_{\mathrm{sq}} + p\psi_{\mathrm{sq}} + \omega_1 \psi_{\mathrm{sd}} \\ v_{\mathrm{rd}} = R_{\mathrm{r}} i_{\mathrm{rd}} + p\psi_{\mathrm{rd}} - \omega_{\mathrm{sl}} \psi_{\mathrm{rq}} \\ v_{\mathrm{rq}} = R_{\mathrm{r}} i_{\mathrm{rq}} + p\psi_{\mathrm{rq}} + \omega_{\mathrm{sl}} \psi_{\mathrm{rd}} \end{cases} \tag{1}$$

$$\begin{cases}\psi_{\rm sd} = L_{\rm s} i_{\rm sd} + L_{\rm m} i_{\rm rd} \\ \psi_{\rm sq} = L_{\rm s} i_{\rm sq} + L_{\rm m} i_{\rm rq} \\ \psi_{\rm rd} = L_{\rm m} i_{\rm sd} + L_{\rm r} i_{\rm rd} \\ \psi_{\rm rq} = L_{\rm m} i_{\rm sq} + L_{\rm r} i_{\rm rq}\end{cases} \tag{2}$$

where p means differential operation. $R_{\rm s}$, $R_{\rm r}$, $L_{\rm s}$, $L_{\rm r}$, and $L_{\rm m}$ are the stator resistance, rotor resistance, stator inductance, rotor inductance, and mutual inductance, respectively. $\Psi_{\rm sd}$, $\Psi_{\rm sq}$, $\Psi_{\rm rd}$, and $\Psi_{\rm rq}$, are the d-q components of stator flux and rotor flux. ω_1 denotes the fundamental angular frequency, i.e., 100π rad/s, and $\omega_{\rm sl} = \omega_1 - \omega_{\rm r}$ is the slip angular frequency.

When the stator resistance is ignored, linearizing (1) and (2), and applying Laplace transformation, the impedance model of the DFIG in the d-q frame can finally be expressed as

$$\boldsymbol{Y}_{\rm dq}^{\rm dfig} = \frac{1}{L_{\rm s}}\boldsymbol{G}_{\rm 1dq} + \frac{L_{\rm m}}{L_{\rm s}}\boldsymbol{G}_{\rm 1dq}\boldsymbol{G}_{\rm 2dq}\boldsymbol{G}_{\rm pdq} \tag{3}$$

$$\boldsymbol{G}_{\rm 1dq} = \begin{bmatrix} \frac{s}{s^2+\omega_1^2} & \frac{\omega_1}{s^2+\omega_1^2} \\ \frac{-\omega_1}{s^2+\omega_1^2} & \frac{s}{s^2+\omega_1^2}\end{bmatrix};\quad \boldsymbol{G}_{\rm 2dq} = \frac{L_{\rm m}}{L_{\rm s}}\begin{bmatrix} s & -\omega_{\rm sl} \\ \omega_{\rm sl} & s\end{bmatrix}$$

$$\boldsymbol{G}_{\rm pdq} = \begin{bmatrix} \frac{(R_{\rm r}+sL_{\rm r}\sigma)}{(R_{\rm r}+sL_{\rm r}\sigma)^2+(\omega_{\rm sl}L_{\rm r}\sigma)^2} & \frac{\omega_{\rm sl}L_{\rm r}\sigma}{(R_{\rm r}+sL_{\rm r}\sigma)^2+(\omega_{\rm sl}L_{\rm r}\sigma)^2} \\ \frac{-\omega_{\rm sl}L_{\rm r}\sigma}{(R_{\rm r}+sL_{\rm r}\sigma)^2+(\omega_{\rm sl}L_{\rm r}\sigma)^2} & \frac{(R_{\rm r}+sL_{\rm r}\sigma)}{(R_{\rm r}+sL_{\rm r}\sigma)^2+(\omega_{\rm sl}L_{\rm r}\sigma)^2}\end{bmatrix} \tag{4}$$

where s denote the Laplace operator and $\sigma = 1 - L_{\rm m}^2/(L_{\rm s}L_{\rm r})$.

It can be found that the diagonal elements of $\boldsymbol{G}_{\rm 1dq}$, $\boldsymbol{G}_{\rm 2dq}$, and $\boldsymbol{G}_{\rm pdq}$ are equal, and their off-diagonal elements are opposite, indicating that the DFIG is a symmetrical system without PLL and RSC, which can also be considered as a SISO system using complex vectors model.

C. Impedance Model of DFIG System With PLL

The influence of PLL on stator voltage, rotor current, and rotor voltage can be derived as [9]

$$\begin{aligned}\boldsymbol{v}_{\rm sdq}^{\rm ctrl} &= \boldsymbol{v}_{\rm sdq} - \boldsymbol{G}_{\rm PLL}^{\rm v}\cdot\boldsymbol{v}_{\rm sdq} \\ \boldsymbol{i}_{\rm rdq}^{\rm ctrl} &= \boldsymbol{i}_{\rm rdq} - \boldsymbol{G}_{\rm PLL}^{\rm i}\cdot\boldsymbol{v}_{\rm sdq} \\ \boldsymbol{v}_{\rm rdq} &= \boldsymbol{v}_{\rm rdq}^{\rm ctrl} + \boldsymbol{G}_{\rm PLL}^{\rm m}\cdot\boldsymbol{v}_{\rm sdq}\end{aligned} \tag{5}$$

where the d-q components all represent the small signal perturbation in the s-domain, and the matrices related to the PLL dynamics can be expressed as

$$\begin{aligned}\boldsymbol{G}_{\rm PLL}^{\rm v} &= \begin{bmatrix}0 & -V_{\rm sq0}H_{\rm pll}(s) \\ 0 & V_{\rm sd0}H_{\rm pll}(s)\end{bmatrix} \\ \boldsymbol{G}_{\rm PLL}^{\rm i} &= \begin{bmatrix}0 & -I_{\rm rq0}H_{\rm pll}(s) \\ 0 & I_{\rm rd0}H_{\rm pll}(s)\end{bmatrix} \\ \boldsymbol{G}_{\rm PLL}^{\rm m} &= \begin{bmatrix}0 & -V_{\rm rq0}H_{\rm pll}(s) \\ 0 & V_{\rm rd0}H_{\rm pll}(s)\end{bmatrix}\end{aligned} \tag{6}$$

where $V_{\rm sd0}$, $V_{\rm sq0}$, $I_{\rm rd0}$, $I_{\rm rq0}$, $V_{\rm rd0}$, and $V_{\rm rq0}$ denote the steady-state values. $H_{\rm pll}(s)$ is a second-order transfer function for the PLL, which can be expressed as [21]

$$H_{\rm pll}(s) = \frac{K_{\rm pPLL}s + K_{\rm iPLL}}{s^2 + K_{\rm pPLL}V_{\rm sd0}s + K_{\rm iPLL}V_{\rm sd0}} \tag{7}$$

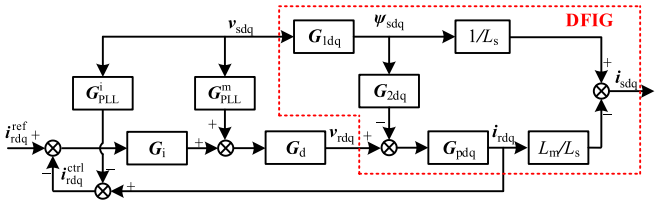

Fig. 2. Impedance model of the DFIG system in the d-q frame with considering PLL.

where $K_{\rm pPLL}$ and $K_{\rm iPLL}$ are the proportional gain and integral gain of the PLL controller, respectively.

Considering the dynamics of PLL, and the rotor current control loop of RSC, the impedance model of the DFIG system can be depicted in Fig. 2. In Fig. 2, $\boldsymbol{G}_{\rm i}$ and $\boldsymbol{G}_{\rm d}$ present the transfer matrices for the PI controller and system delay in the RSC current control loop.

According to Fig. 2, the admittance of the DFIG system in the d-q frame can be deduced as

$$\begin{aligned}\boldsymbol{Y}_{\rm dq}^{\rm dfrc} &= \frac{\boldsymbol{i}_{\rm sdq}}{\boldsymbol{v}_{\rm sdq}} \\ &= \underbrace{\frac{1}{L_{\rm s}}\boldsymbol{G}_{\rm 1dq} + \frac{L_{\rm m}}{L_{\rm s}}(\boldsymbol{I}+\boldsymbol{G}_{\rm pdq}\boldsymbol{G}_{\rm d}\boldsymbol{G}_{\rm i})^{-1}\boldsymbol{G}_{\rm pdq}\boldsymbol{G}_{\rm 2dq}\boldsymbol{G}_{\rm 1dq}}_{\boldsymbol{Y}_{\rm dq}^{\rm SISO}} \\ &\quad \underbrace{-\frac{L_{\rm m}}{L_{\rm s}}(\boldsymbol{I}+\boldsymbol{G}_{\rm pdq}\boldsymbol{G}_{\rm d}\boldsymbol{G}_{\rm i})^{-1}\boldsymbol{G}_{\rm pdq}\boldsymbol{G}_{\rm d}\boldsymbol{G}_{\rm i}\boldsymbol{G}_{\rm PLL}^{\rm i}}_{\boldsymbol{Y}_{\rm dq}^{\rm i}} \\ &\quad \underbrace{-\frac{L_{\rm m}}{L_{\rm s}}(\boldsymbol{I}+\boldsymbol{G}_{\rm pdq}\boldsymbol{G}_{\rm d}\boldsymbol{G}_{\rm i})^{-1}\boldsymbol{G}_{\rm pdq}\boldsymbol{G}_{\rm d}\boldsymbol{G}_{\rm PLL}^{\rm m}}_{\boldsymbol{Y}_{\rm dq}^{\rm m}}.\end{aligned} \tag{8}$$

From (8), it can be seen that $\boldsymbol{Y}_{\rm dq}^{\rm dfrc}$ consists of three parts, i.e., $\boldsymbol{Y}_{\rm dq}^{\rm SISO}$, $\boldsymbol{Y}_{\rm dq}^{\rm i}$, and $\boldsymbol{Y}_{\rm dq}^{\rm m}$. $\boldsymbol{Y}_{\rm dq}^{\rm SISO}$ is symmetrical and can be transferred to a SISO impedance using a complex vector model. The effects of PLL on rotor current and rotor voltage are included in $\boldsymbol{Y}_{\rm dq}^{\rm i}$ and $\boldsymbol{Y}_{\rm dq}^{\rm m}$. Therefore, the contributions of $\boldsymbol{Y}_{\rm dq}^{\rm i}$ and $\boldsymbol{Y}_{\rm dq}^{\rm m}$ to the frequency-coupling phenomena can be studied separately.

On this basis, the admittance of the DFIG system in the d-q frame can be further converted in the stationary domain as [22]

$$\boldsymbol{Y}_{\alpha\beta}^{\rm dfrc}(s) = \frac{1}{2}\begin{bmatrix}1 & j \\ 1 & -j\end{bmatrix}\boldsymbol{Y}_{\rm dq}^{\rm dfrc}(s-j\omega_1)\begin{bmatrix}1 & 1 \\ -j & j\end{bmatrix}. \tag{9}$$

Similarly, the admittances $\boldsymbol{Y}_{\alpha\beta}^{\rm SISO}$, $\boldsymbol{Y}_{\alpha\beta}^{\rm i}$, and $\boldsymbol{Y}_{\alpha\beta}^{\rm m}$ in the stationary domain can also be obtained, and the relationship between them can be expressed as

$$\boldsymbol{Y}_{\alpha\beta}^{\rm dfrc} = \boldsymbol{Y}_{\alpha\beta}^{\rm SISO} + \boldsymbol{Y}_{\alpha\beta}^{\rm i} + \boldsymbol{Y}_{\alpha\beta}^{\rm m}. \tag{10}$$

D. Verification and Analysis of the Impedance Model

The simulation model of a DFIG system with PLL under a weak grid is developed in MATLAB/Simulink, and the detailed parameters are shown in Table I.

TABLE I
PARAMETERS OF THE SYSTEM

Symbol	Parameter	Value
U_N	Rated voltage	1 p.u.(690 V)
P_N	Rated power	1 p.u. (1.5 MW)
f_1	Fundamental frequency	1 p.u. (50 Hz)
f_r	Rotor frequency	1.1 p.u. (55 Hz)
n_p	Pole pairs	2
V_{dc}	DC-link voltage	1 p.u. (1150 V)
L_{ls}	Stator leakage	0.059 p.u.
L_{lr}	Rotor leakage	0.082 p.u.
L_{ms}	Mutual inductance	2.919 p.u.
R_s	Stator resistance	0.0076 p.u.
R_r	Rotor resistance	0.0063 p.u.
K_e	Turns ratio	0.33
T_s	Switching period	0.1 ms
f_s	Switching frequency	10 kHz
f_{pll}	Bandwidth of the PLL controller	20 Hz
f_i	Bandwidth of the current controller	430 Hz
SCR	Short-circuit ratio	2

The closed-loop transfer function of the PLL can be written as [23]

$$G_{\mathrm{PLL}}(s)=\frac{\Delta\theta_{\mathrm{pll}}}{\Delta\theta_{\mathrm{s}}}=V_{\mathrm{sd0}}\frac{K_{\mathrm{pPLL}}s+K_{\mathrm{iPLL}}}{s^2+K_{\mathrm{pPLL}}V_{\mathrm{sd0}}s+K_{\mathrm{iPLL}}V_{\mathrm{sd0}}}. \tag{11}$$

When K_{pPLL} and K_{iPLL} are set as 0.153 and 6.618 in this article, the bandwidth of PLL is calculated as 20 Hz. Meanwhile, the bandwidth of the current controller can be estimated through its simplified SISO closed-loop transfer function, which can be expressed as

$$G_{\mathrm{bi}}(s)\approx\frac{G_{\mathrm{i}}(s)G_{\mathrm{pdq}}(s)}{1+G_{\mathrm{i}}(s)G_{\mathrm{pdq}}(s)}=\frac{sK_{\mathrm{pI}}+K_{\mathrm{iI}}}{s^2L_{\mathrm{r}}\sigma+s\left(R_{\mathrm{r}}+K_{\mathrm{pI}}\right)+K_{\mathrm{iI}}}. \tag{12}$$

In this article, K_{pI} and K_{iI} are 5 and 500, respectively, and the bandwidth is estimated as 430 Hz.

Moreover, the equivalent resistance and inductance of the grid is determined by the SCR, and the relationship between them can be written as [24]

$$\begin{cases}R_{\mathrm{g}}=\mathrm{Ratio}\dfrac{U_{\mathrm{N}}^2}{\mathrm{SCR}\cdot P_{\mathrm{N}}\sqrt{1+\mathrm{Ratio}^2}}\\ L_{\mathrm{g}}=\dfrac{U_{\mathrm{N}}^2}{\omega_1\mathrm{SCR}\cdot P_{\mathrm{N}}\sqrt{1+\mathrm{Ratio}^2}}\end{cases} \tag{13}$$

where P_N and U_N are the rated power and rated line voltage of the DFIG system, respectively. The Ratio represents the ratio of grid resistance and grid reactance, i.e., R_g/X_g, which is set as 0.01 in this article.

To verify the accuracy of the DFIG impedance model deduced in (9) and (10), a frequency-sweeping test is carried out in the stationary frame for the convenience of disturbance measurement and impedance characteristic analysis. By injecting positive or negative sequence voltage disturbance at the PCC and detecting the corresponding current disturbance, the simulation results of $\boldsymbol{Y}_{\alpha\beta}^{\mathrm{dfrc}}$ can be calculated. As shown in Fig. 3, the analytical model of the DFIG system, i.e., $\boldsymbol{Y}_{\alpha\beta}^{\mathrm{dfrc}}$, matches the simulation results well, which validates the correctness of the DFIG impedance model.

Moreover, the analytical models for different parts combinations are also given in Fig. 3. From there, it can be seen that the Bode diagram of $\boldsymbol{Y}_{\alpha\beta}^{\mathrm{SISO}}+\boldsymbol{Y}_{\alpha\beta}^{\mathrm{i}}$ is almost coincident with $\boldsymbol{Y}_{\alpha\beta}^{\mathrm{dfrc}}$, indicating $\boldsymbol{Y}_{\alpha\beta}^{\mathrm{m}}$ has little influence on the MIMO admittance of the DFIG system. Nevertheless, the diagonal elements of $\boldsymbol{Y}_{\alpha\beta}^{\mathrm{SISO}}+\boldsymbol{Y}_{\alpha\beta}^{\mathrm{m}}$ are coincident with $\boldsymbol{Y}_{\alpha\beta}^{\mathrm{SISO}}$ and the off-diagonal elements of it decrease to below -20 dB, which is much lower than the diagonal elements and can almost be neglected. Therefore, the frequency-coupling phenomena caused by the PLL are mainly related to $\boldsymbol{Y}_{\alpha\beta}^{\mathrm{i}}$. When $\boldsymbol{Y}_{\alpha\beta}^{\mathrm{i}}$ is ignored, the influence of the PLL will be greatly reduced, and the whole DFIG system can be approximately regarded as a SISO system using a complex vector model.

The rated power of the DFIG is about or beyond 1.5 MW, and its rated voltage is about 690 V (960 V for higher power DFIG), which leads to the rated current being much greater than the rated voltage, especially on the rotor side. Thus, the steady-state values in $\boldsymbol{G}_{\mathrm{PLL}}^{\mathrm{i}}$ will be much greater than those in $\boldsymbol{G}_{\mathrm{PLL}}^{\mathrm{m}}$, finally, resulting in $\boldsymbol{Y}_{\alpha\beta}^{\mathrm{i}}$ contributing more than $\boldsymbol{Y}_{\alpha\beta}^{\mathrm{m}}$to frequency-coupling phenomena.

III. IMPEDANCE RESHAPING METHOD

A. Proposal of Impedance Reshaping Method

The abovementioned analysis shows that the frequency-coupling phenomena are mainly caused by $\boldsymbol{Y}_{\alpha\beta}^{\mathrm{i}}$, which is dominated by the matrix $\boldsymbol{G}_{\mathrm{PLL}}^{\mathrm{i}}$ that is related to the rotor current dynamic. Therefore, this article tries to use a parallel impedance reshaping path to compensate for the rotor current dynamic caused by PLL, thus eliminating the influence of $\boldsymbol{G}_{\mathrm{PLL}}^{\mathrm{i}}$, as shown in Fig. 4. It can be seen that the introduced path includes two blocks, i.e., $\boldsymbol{I}-\boldsymbol{G}_{\mathrm{PLL}}^{\mathrm{v}}$ and $\boldsymbol{G}_{\mathrm{z}}$. As $\boldsymbol{I}-\boldsymbol{G}_{\mathrm{PLL}}^{\mathrm{v}}$ necessary for transforming the stator voltage to the control d-q frame; thus, only $\boldsymbol{G}_{\mathrm{z}}$ should be designed.

In order to eliminate the influence of $\boldsymbol{G}_{\mathrm{PLL}}^{\mathrm{i}}$, the following relationship needs to be satisfied:

$$\boldsymbol{G}_{\mathrm{z}}=\boldsymbol{G}_{\mathrm{PLL}}^{\mathrm{i}}\left(\boldsymbol{I}-\boldsymbol{G}_{\mathrm{PLL}}^{\mathrm{v}}\right)^{-1}=\begin{bmatrix}0 & -I_{\mathrm{rq0}}\left(K_{\mathrm{pPLL}}s+K_{\mathrm{iPLL}}\right)/s^2\\ 0 & I_{\mathrm{rd0}}\left(K_{\mathrm{pPLL}}s+K_{\mathrm{iPLL}}\right)/s^2\end{bmatrix} \tag{14}$$

where $\boldsymbol{I}$ represents a 2×2 identity matrix.

From (14), it can be seen that $\boldsymbol{G}_{\mathrm{z}}$ has an asymmetric structure, and its nonzero elements exist only in the second column, which is related to $v_{\mathrm{sq}}^{\mathrm{ctrl}}$. Besides, $\boldsymbol{G}_{\mathrm{z}}$ is similar to a second-order integral term, and the dc components of $v_{\mathrm{sq}}^{\mathrm{ctrl}}$ will be amplified, causing the rotor current to deviate from its expected values. Thus, it is necessary to add a second-order high-pass filter (HPF) in the reshaping branch to remove the dc components of $v_{\mathrm{sq}}^{\mathrm{ctrl}}$. At the same time, to improve the adaptability of the proposed method, the steady-state values can be replaced by reference values, i.e., $\boldsymbol{I}_{\mathrm{rdqref}}$. As a result, $\boldsymbol{G}_{\mathrm{z}}$ can be deduced as

$$\boldsymbol{G}_{\mathrm{z1}}=G_{\mathrm{HPF}}(s)\begin{bmatrix}0 & -I_{\mathrm{rqref}}\left(K_{\mathrm{pPLL}}s+K_{\mathrm{iPLL}}\right)/s^2\\ 0 & I_{\mathrm{rdref}}\left(K_{\mathrm{pPLL}}s+K_{\mathrm{iPLL}}\right)/s^2\end{bmatrix} \tag{15}$$

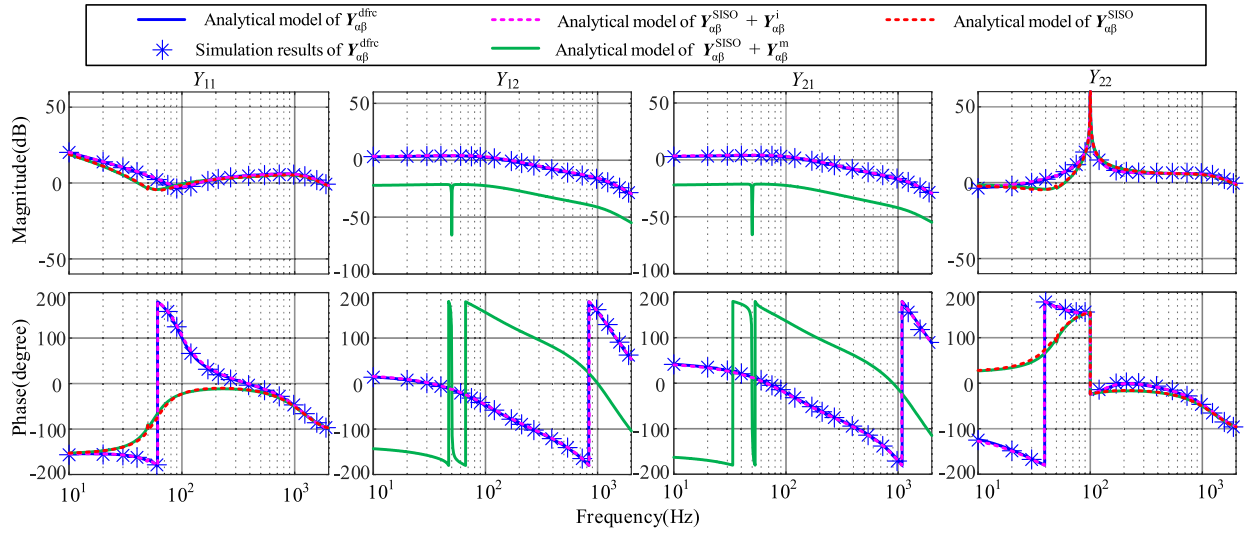

Fig. 3. Comparison of the DFIG impedance models with different parts of combinations.

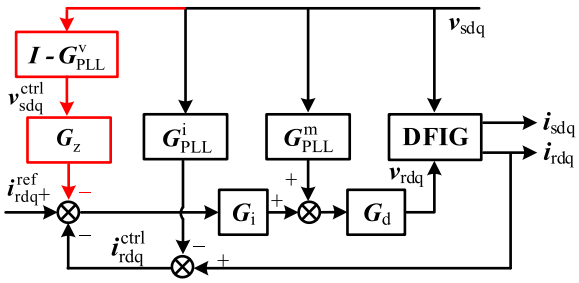

Fig. 4. Control diagram of the DFIG system with reshaping to reduce the frequency-coupling phenomenon.

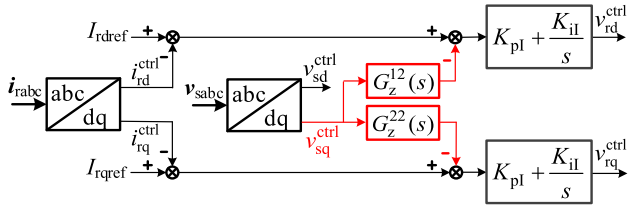

Fig. 5. Implementation diagram of the RSC current controller with adopting the proposed methods.

where $G_{\mathrm{HPF}}(s)$ represents the transfer function of the second-order HPF, which can be written as

$$G_{\mathrm{HPF}}(s)=\frac{A(\infty)s^2}{s^2+(\omega_{\mathrm{HPF}}/Q)\,s+\omega_{\mathrm{HPF}}^2}. \tag{16}$$

Generally, the dc component can be almost attenuated by using the HPF filter with any corner frequency ω_{HPF}. However, a higher ω_{HPF} will worsen the decoupling effect of the proposed method. To ensure the HPF will not greatly affect the decoupling function of the reshaping method, ω_{HPF} should be small, which is set to $2\pi\cdot1$ rad/s in this article. Accordingly, the gain coefficient $A(\infty)$ and the quality factor Q are both set as 1.

For the DFIG system, most of the oscillations usually occur beyond 50 Hz [25]. Thus, the high-frequency range, i.e., above 50 Hz, is mainly in focus here. In this frequency range, if in some cases $K_{\mathrm{pPLL}}s$ are much greater than K_{iPLL}, the integral gain K_{iPLL} can thus be ignored for simplification. To this end, the reshaping method in (15) can be further simplified as

$$\boldsymbol{G}_{\mathrm{z2}}=\frac{s}{s+\omega_{\mathrm{HPF}}}\begin{bmatrix}0 & \frac{-I_{\mathrm{rqref}}K_{\mathrm{pPLL}}}{s}\\ 0 & \frac{I_{\mathrm{rdref}}K_{\mathrm{pPLL}}}{s}\end{bmatrix}=\begin{bmatrix}0 & \frac{-I_{\mathrm{rqref}}K_{\mathrm{pPLL}}}{s+\omega_{\mathrm{HPF}}}\\ 0 & \frac{I_{\mathrm{rdref}}K_{\mathrm{pPLL}}}{s+\omega_{\mathrm{HPF}}}\end{bmatrix}. \tag{17}$$

Finally, the original second-order reshaping method becomes a first-order one, and only a first-order HPF is required. By further derivation, just a pair of asymmetrical low-pass filters (LPF) should be added, which greatly decreases the implementation complexity. The implementation diagram is shown in Fig. 5, where the reshaping branch is plotted in red. $G_{\mathrm{z}}^{12}(\mathrm{s})$ and $G_{\mathrm{z}}^{22}(\mathrm{s})$represent the second-column elements of $\boldsymbol{G}_{\mathrm{z1}}$ or $\boldsymbol{G}_{\mathrm{z2}}$. K_{pI} and K_{iI} denote the proportional gain and integral gain of the current controller, respectively.

It should be noted that the compensation methods for the rotor current dynamic in this article are proposed to cancel frequency-coupling phenomena and reshape the impedance model, resulting in stability improvement. This is different from the existing methods based on the voltage feedforward or adding particular filters in the voltage feedforward branches [26], [27], where the feedforward terms are usually behind the current PI controller and used to optimize impedance characteristics or improve the response of tracking reference signal. In this article, the reshaping terms are added before the PI controller to compensate for the dynamic of the rotor current, thus reducing the influence of PLL. Meanwhile, the proposed methods have design-oriented parameters.

B. Stability Analysis

The stability of the DFIG interconnected system can be assessed through the generalized Nyquist criterion (GNC) [28],

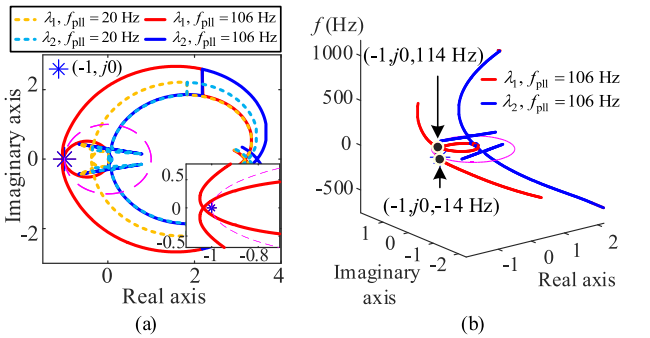

Fig. 6. Nyquist diagram of the DFIG interconnected system. (a) PLL bandwidth increases from 20 to 106 Hz. (b) Enlarged 3-D view for the PLL bandwidth is 106 Hz.

i.e., analyzing the eigen-loci, which can be calculated as

$$\det(\lambda \boldsymbol{I} - \boldsymbol{Y}_{\alpha\beta}^{\mathrm{dfrc}} \boldsymbol{Z}_{\mathrm{g}}) = 0 \tag{18}$$

where $\boldsymbol{Z}_{\mathrm{g}}$ represents the grid impedance matrix [29].

Assuming the DFIG interconnected system operates at the rated power, as shown in Table I. Fig. 6 shows the generalized Nyquist plots of the system when the bandwidth of PLL increases from 20 to 106 Hz with SCR = 2.

From Fig. 6(a), it can be seen that when the PLL bandwidth is 20 Hz, the eigen-loci of the system do not encircle the critical point $(-1, j0)$, representing that the system is stable. However, when the PLL bandwidth increases to 106 Hz, the $(-1, j0)$ point is encircled, indicating an oscillation will occur. From the enlarged 3D-view Nyquist diagram in Fig. 6(b), the oscillation frequencies are about 114 and -14 Hz, which is consistent with the frequency-coupling phenomena mentioned in [22].

In order to acquire the stability margin of the system directly, the equivalent SISO impedance model [30] of the interconnected system should be deduced, which is derived from the closed-loop stability criterion of the MIMO system

$$\begin{cases} Z_{\mathrm{peq}} = Z_{11} - Z_{12}\dfrac{Z_{21}+Z_{\mathrm{g}21}}{Z_{22}+Z_{\mathrm{g}22}} \\ Z_{\mathrm{pgeq}} = Z_{\mathrm{g}11} - Z_{\mathrm{g}12}\dfrac{Z_{21}+Z_{\mathrm{g}21}}{Z_{22}+Z_{\mathrm{g}22}} \end{cases} \tag{19}$$

where Z_{11}, Z_{12}, Z_{21}, Z_{22}, $Z_{\mathrm{g}11}$, $Z_{\mathrm{g}12}$, $Z_{\mathrm{g}21}$, and $Z_{\mathrm{g}22}$, are the elements of $(\boldsymbol{Y}_{\alpha\beta}^{\mathrm{dfrc}})^{-1}$ and $\boldsymbol{Z}_{\mathrm{g}}$, respectively. The subscript numbers represent the corresponding row and column position. Considering the off-diagonal elements of $\boldsymbol{Z}_{\mathrm{g}}$, i.e., $Z_{\mathrm{g}12}$ and $Z_{\mathrm{g}21}$, are zeros, the equivalent SISO impedance in (19) can be further simplified as

$$\begin{cases} Z_{\mathrm{peq}} = Z_{11} - \dfrac{Z_{21}Z_{12}}{Z_{22}+Z_{\mathrm{g}22}} \\ Z_{\mathrm{pgeq}} = Z_{\mathrm{g}11} \end{cases}. \tag{20}$$

Using the same methods, the negative-sequence equivalent SISO impedances can also be obtained, and the stability of the system can be checked by the Nyquist criterion of the SISO system. For simplification, only the positive-sequence impedance Z_{peq} and Z_{pgeq} is considered and the analysis of Z_{ngeq} and Z_{neq} is ignored in later sections. Meanwhile, from (20), it can be seen that the system will be a real SISO system, i.e., $Z_{\mathrm{peq}} = Z_{11}$ and

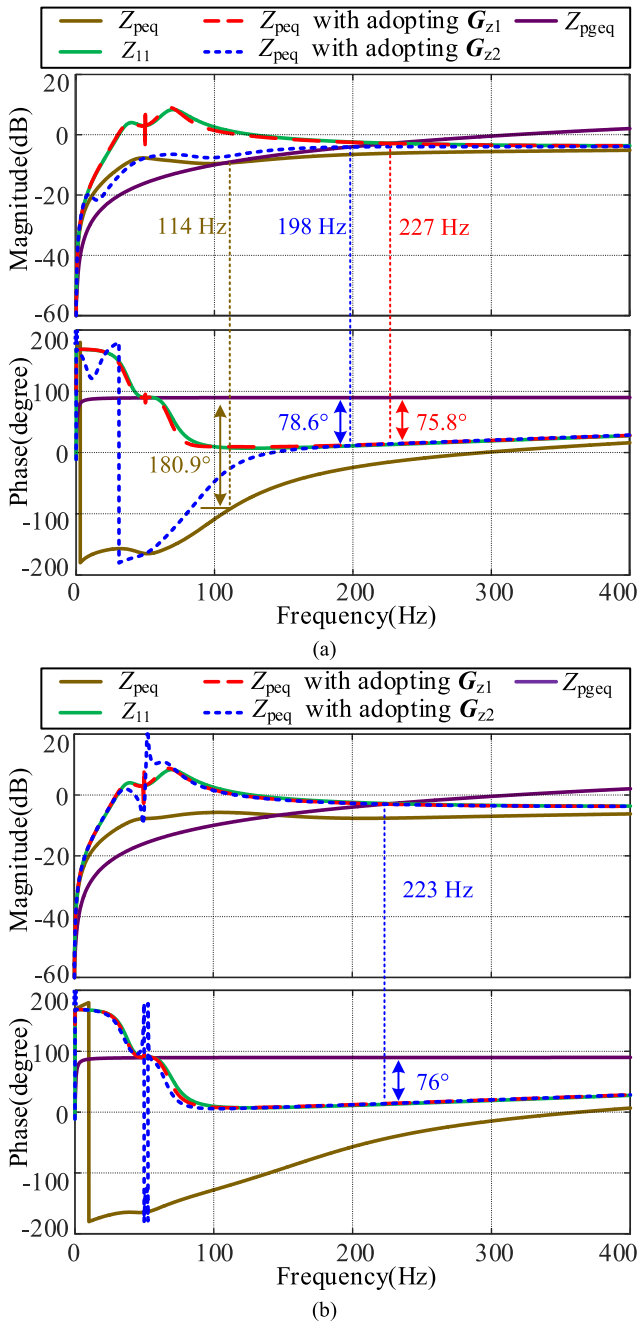

Fig. 7. Bode diagram of the positive-sequence equivalent SISO impedance model with adopting proposed reshaping methods when the PLL bandwidth is 106 Hz. (a) $K_{\mathrm{pPLL}} = 0.812$ and $K_{\mathrm{iPLL}} = 185.893$. (b) $K_{\mathrm{pPLL}} = 1.176$ and $K_{\mathrm{iPLL}} = 4.092$.

$Z_{\mathrm{neq}} = Z_{22}$, when the frequency-coupling effect is eliminated. In other words, $Z_{12} \approx 0$ and $Z_{21} \approx 0$.

The Bode diagram of the positive-sequence equivalent SISO impedance model with or without adopting the proposed methods is given in Fig. 7. When the PLL bandwidth is 106 Hz, from Fig. 7(a), the amplitude–frequency characteristic curves of Z_{peq} and Z_{pgeq} intersect at 114 Hz, and the corresponding phase difference is 180.9°, indicating an oscillation will happen at positive 114 Hz. Meanwhile, an oscillation at negative

14 Hz will also happen, concluded by the negative-sequence impedance model. The results also agree well with the analysis using the MIMO impedance model in Fig. 6. Fortunately, when the reshaping method $\boldsymbol{G}_{z1}$ is adopted, the Bode diagram of Z_{peq} is coincident with the curves of Z_{11}, indicating that the frequency-coupling effect was almost eliminated. Meanwhile, the negative-resistance region can be removed, and the stability of the system is improved a lot, as seen in Fig. 7(a). The intersection frequency increases to 227 Hz, and the corresponding phase difference decreases to 75.8°.

When the simplified method $\boldsymbol{G}_{z2}$ is adopted, from Fig. 7(a), the negative-resistance region of Z_{peq} will be also reduced. Therefore, the phase difference decreases to 78.6° at the intersection frequency 198 Hz, resulting in the stability margin of the system increasing a lot. Keeping $f_{pll} = 106$ Hz, if K_{pPLL} increases to 1.176, i.e., $K_{pPLL}s \gg K_{iPLL}$ is almost satisfied, the Bode diagram of Z_{peq} with adopting $\boldsymbol{G}_{z2}$ will also be coincident with Z_{11}, as shown in Fig. 7(b). From here, it can be seen that the negative-resistance region will be removed, showing $\boldsymbol{G}_{z2}$ plays the same role as $\boldsymbol{G}_{z1}$ under this condition.

The earlier analysis indicates that $\boldsymbol{G}_{z1}$ and $\boldsymbol{G}_{z2}$ can both improve the stability of the DFIG system. Meanwhile, $\boldsymbol{G}_{z1}$ can almost remove all the negative-resistance regions under any conditions while $\boldsymbol{G}_{z2}$ can only achieve this when K_{pPLL} is relatively large.

IV. Robust Analysis

When the DFIG system is connected to a weak grid, the system parameters may vary, such as SCR, active and reactive power requirements, rotor frequency, DFIG leakage inductance, controller bandwidth, etc. Therefore, it is necessary to analyze the robustness of the proposed methods against the system parameters or operating condition variations.

Combining the voltage and flux equations mentioned in (1) and (2) as well as R_g and L_g derived in (13), it can be found that the steady-state algebraic equations of the DFIG system have no solution when SCR < 2. Therefore, SCR $= 2$ is regarded as the worst grid condition. Since the methods are proven to be effective with SCR $= 2$, it is only necessary to study the effectiveness of the methods when SCR increases. When $\boldsymbol{G}_{z1}$ or $\boldsymbol{G}_{z2}$ is employed, the Bode diagrams of Z_{peq} with different SCR are given in Fig. 8. From Fig. 8, when the SCR increases to 5, the amplitude–frequency curves of Z_{peq} and Z_{pgeq} will intersect at about 524 Hz, and the phase difference is 51.3°, denoting the system is quite stable. Meanwhile, the intersection frequency of Z_{peq} and Z_{pgeq} will be much higher when the SCR increases to 10, where the DFIG system is in a positive resistance region, and the system has no risk of oscillation. The previous analysis implies that as long as the parameters of the impedance reshaping methods are designed for the lowest SCR, the system can still keep stable when the SCR varies.

The robust analysis against other parameter deviations, such as power requirements, rotor frequency, DFIG leakage inductance, and controller bandwidth, is also investigated, by plotting and analyzing the Bode diagram of Z_{peq} and Z_{pgeq}, just like the process in Fig. 8. The corresponding results are shown in Table II. Generally, the power factor of the DFIG is kept between 0.95 and 1. However, when the voltage sag occurs, additional reactive power is required by DFIG to support the PCC voltage. As it can be seen from Table II, when DFIG operates at the power factor of 0.95 or generates reactive power at -1 p.u., the phase differences are both smaller than 180° at the intersection frequency, meaning both methods still do well when the power requirements vary in a prospective range. Similarly, a different rotor frequency range (deviating ±20%), which is equivalent to the rotor speed deviating ±20%, as well as DFIG leakage inductance deviating ±20% from the rated value is analyzed, and the phase differences are also calculated for the intersection frequency. It can be found that the phase differences are still far less than 180°, implying that $\boldsymbol{G}_{z1}$ and $\boldsymbol{G}_{z2}$ are both effective for rotor frequency and leakage inductance varying in a normal range.

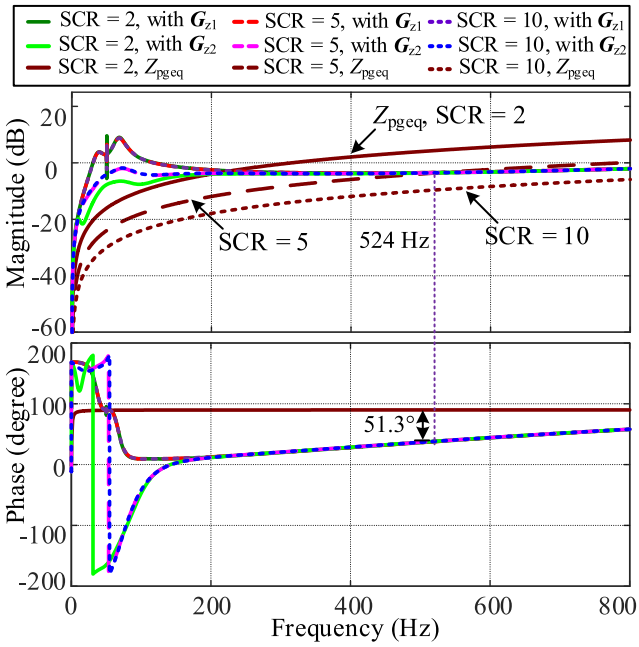

Fig. 8. Bode diagram of the positive-sequence equivalent SISO impedance model of the DFIG system adopting the reshaping methods with different SCRs.

Besides, the controller bandwidth can also be modified to make the DFIG system acquire different dynamic characteristics. As seen in Table II, when the current controller bandwidth is changed to 300 or 500 Hz, the critical PLL bandwidth of oscillation will change to 108 and 105 Hz, respectively. If $\boldsymbol{G}_{z1}$ or $\boldsymbol{G}_{z2}$ is adopted, the system is stabilized, and the phase differences will be far less than 180° at the intersection frequencies, denoting both reshaping methods are effective even if controller bandwidth varies.

V. Experimental Verification

To further verify the effectiveness of the proposed impedance reshaping methods, a control-hardware-in-the-loop experiment based on a DSP+FPGA control board and RT-LAB real-time digital simulation platform is carried out, as shown in Fig. 9.

TABLE II
ROBUSTNESS ANALYSIS RESULTS AGAINST PARAMETERS DEVIATION

Robustness analysis against power reference deviations		
Method	Power requirements	Intersection frequency and phase difference
$\boldsymbol{G}_{z1}$	$P_{ref}=0$ p.u., $Q_{ref}=-1$ p.u.	226 Hz / 74.6 °
	$P_{ref}=-0.95$ p.u., $Q_{ref}=-0.31$ p.u.	225 Hz / 75.2 °
	$P_{ref}=-0.95$ p.u., $Q_{ref}=0.31$ p.u.	224 Hz / 76.1 °
$\boldsymbol{G}_{z2}$	$P_{ref}=0$ p.u., $Q_{ref}=-1$ p.u.	216 Hz/ 69.5 °
	$P_{ref}=-0.95$ p.u., $Q_{ref}=-0.31$ p.u.	203 Hz / 75.5 °
	$P_{ref}=-0.95$ p.u., $Q_{ref}=0.31$ p.u.	197 Hz / 78.2 °
Robustness analysis against rotor frequency deviations		
Method	Rotor frequency	Intersection frequency and phase difference
$\boldsymbol{G}_{z1}$	60 Hz	230 Hz / 74.8 °
	40 Hz	216 Hz / 78.8 °
$\boldsymbol{G}_{z2}$	60 Hz	201 Hz / 77.6 °
	40 Hz	183 Hz / 82.7 °
Robustness analysis against leakage inductance deviations		
Method	DFIG leakage inductance deviation	Intersection frequency and phase difference
$\boldsymbol{G}_{z1}$	+20%	227 Hz / 71.9 °
	-20%	226 Hz / 79.0 °
$\boldsymbol{G}_{z2}$	+20%	197 Hz / 75.9 °
	-20%	196 Hz / 80.7 °
Robustness analysis against controller bandwidth deviations		
Method	Bandwidth of RSC current controller and critical f_{pll}	Intersection frequency and phase difference
$\boldsymbol{G}_{z1}$	$f_i=300$ Hz, $f_{pll}=108$ Hz	172 Hz / 74.7 °
	$f_i=500$ Hz, $f_{pll}=105$ Hz	254 Hz / 76.8 °
$\boldsymbol{G}_{z2}$	$f_i=300$ Hz, $f_{pll}=108$ Hz	121 Hz / 98.9 °
	$f_i=500$ Hz, $f_{pll}=105$ Hz	229 Hz / 78.1 °

The system parameters are the same as theoretical analysis, which are listed in Table I.

Fig. 10(a) shows the experimental waveforms of stator voltage, rotor current, as well as the active and reactive power of the DFIG system. In the beginning, $f_{pll}=20$ Hz, and the system is stable. At $t=t_1$, f_{pll} increases to 106 Hz the system loses its stability and an oscillation occurs. Fast Fourier transformation (FFT) was performed for stator voltage during t_1-t_2 when the oscillation happens, the corresponding FFT results are shown in Fig. 10(b). From there, it can be seen that the oscillation frequencies are 114 and 14 Hz, which is consistent with the theoretical analysis results in Fig. 6. Fortunately, when the reshaping method $\boldsymbol{G}_{z1}$ is added at t_2, from Fig. 10(a), it can be seen that the oscillation is significantly suppressed and the system becomes stable. Then switching $\boldsymbol{G}_{z1}$ to $\boldsymbol{G}_{z2}$ at t_3, the system still keeps stable, implying that $\boldsymbol{G}_{z2}$ can also suppress the oscillation. The experimental results greatly demonstrate the correctness of the theoretical analysis and the effectiveness of the proposed methods.

The robustness of the reshaping methods against the deviations of SCR, power requirements, rotor frequency, and controller bandwidth are all tested by experiment. The results

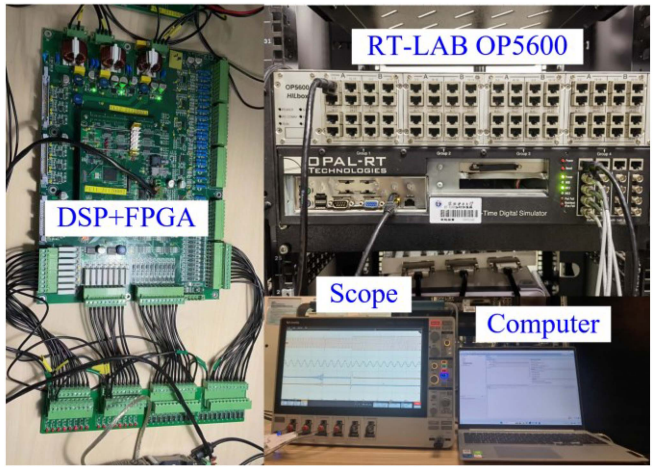

Fig. 9. Control hardware-in-the-loop experiment platform.

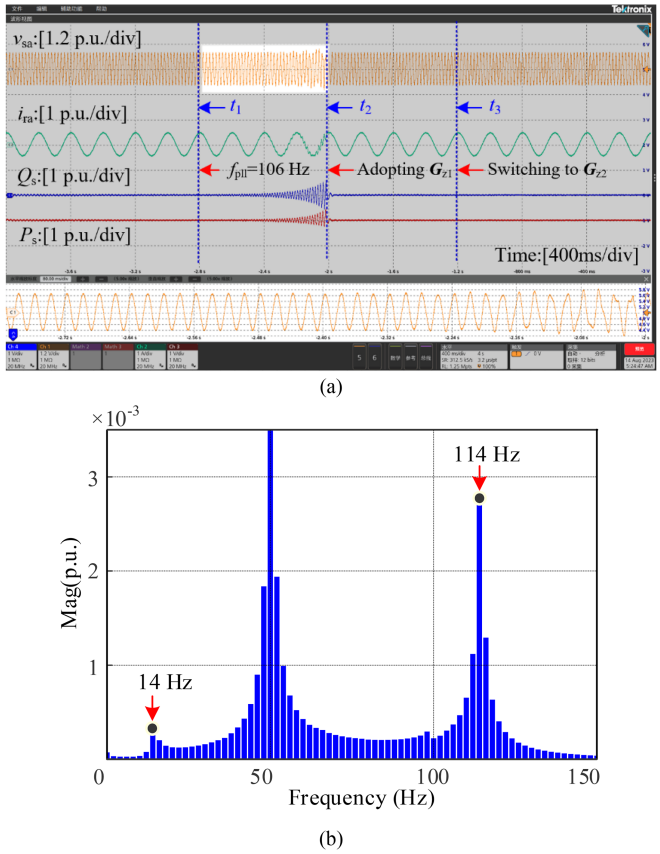

Fig. 10. Experimental waveforms of applying the reshaping methods and FFT analysis results. (a) Experimental waveforms of the DFIG system. (b) FFT analysis results of the stator voltage waveform during t_1–t_2.

are shown in Figs. 11–14, respectively. In Figs. 11–13, the experimental waveforms of the system before $t=t_2$ are the same as that in Fig. 10(a). From Fig. 11, $\boldsymbol{G}_{z2}$ is introduced first at t_2, and the oscillation is suppressed and the system operates stably, indicating that $\boldsymbol{G}_{z2}$ can also be used to remove the oscillation caused by PLL. Then, SCR jumps from 2 to 10 at t_3, and the system is still stabilized, which is consistent with the theoretical

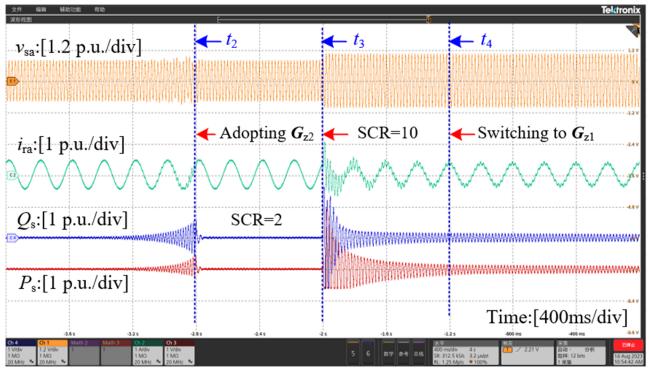

Fig. 11. Experimental results of applying the reshaping methods when SCR varies.

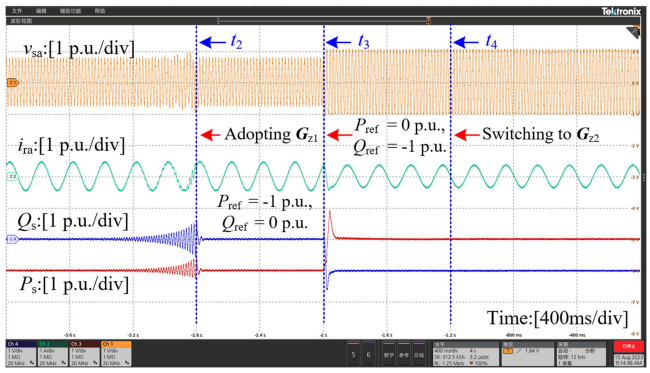

Fig. 12. Experimental results of applying the reshaping methods when DFIG power references vary.

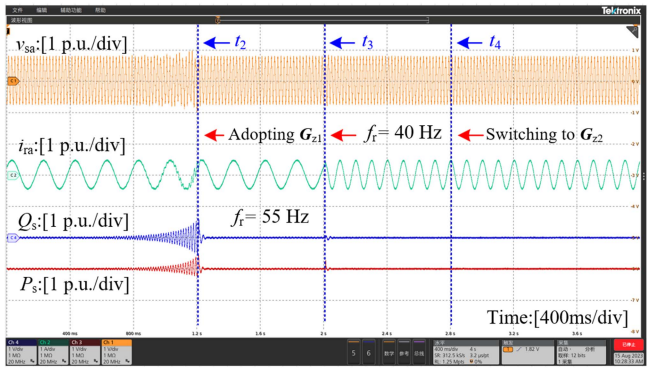

Fig. 13. Experimental results of applying the reshaping methods when the rotor frequency varies.

analysis in Fig. 8. Finally, switching $\boldsymbol{G}_{z2}$ to $\boldsymbol{G}_{z1}$ at t_4, the system still remains stable. The previous experimental results prove that both reshaping methods can reduce the influence of PLL and improve the stability margin of the system even when SCR varies.

In Fig. 12, P_{ref} is changed from -1 to 0 p.u. and Q_{ref} is changed from 0 to -1 p.u. at t_3. It can be seen that $\boldsymbol{G}_{z1}$ can still effectively suppress the oscillation even if the active and reactive power references are reversed. Later, switching the reshaping

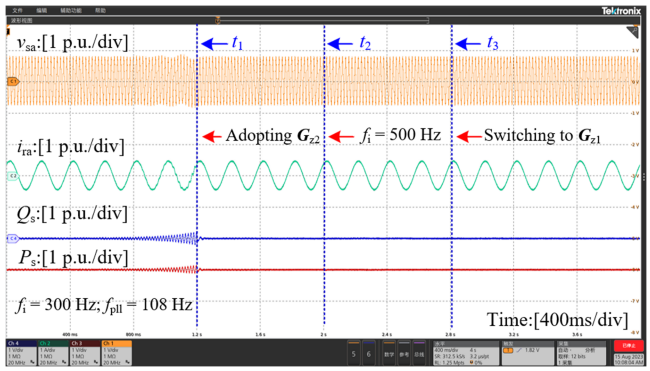

Fig. 14. Experimental results of applying the reshaping methods when the controller bandwidth varies.

method $\boldsymbol{G}_{z1}$ to $\boldsymbol{G}_{z2}$ at t_4, it can be observed that the system keeps stable. The experimental results agree with the robust analysis against power requirement deviations in Section IV, indicating both methods can still reduce the influence of PLL and improve the stability margin of the DFIG system when power references vary. It should also be mentioned that, in Figs. 11 and 12, when SCR or power references jump at t_3, the real current will be not equal to the current references in a short time. Fortunately, due to the great stability improvement effect of the proposed methods, the real current finally follows the references through the PI controller, which also proves the effectiveness of the proposed methods in dynamic processes.

In Fig. 13, at $t = t_3$, the rotor frequency changes from 55 to 40 Hz, and the DFIG system operates from supersynchronous speed to subsynchronous speed. According to Fig. 13, the system remains stable after the rotor frequency varies, and the stator output power is finally adjusted to the expected values. Then, changing the reshaping method from $\boldsymbol{G}_{z1}$ to $\boldsymbol{G}_{z2}$ at t_4, the system is also stabilized. The result verifies the robustness analysis against rotor frequency deviations, showing that both methods still have good performance during rotor frequency variations.

As shown in Fig. 14, at the beginning, the bandwidth of the current controller is 300 Hz. When the PLL bandwidth increases to 108 Hz, the oscillation occurs, and the system loses its stability, which agrees well with the theoretical results presented in Table II. Adopting $\boldsymbol{G}_{z2}$ at $t = t_1$, the oscillation is suppressed. f_i jumps to 500 Hz at t_2, and the system remains stable, which indicates that $\boldsymbol{G}_{z2}$ is still effective when the controller bandwidth varies. Then, switching $\boldsymbol{G}_{z2}$ to $\boldsymbol{G}_{z1}$ at t_3, the system is still stable. The experimental results prove that both methods can still reduce the influence of PLL and improve the stability margin of the DFIG system when the controller bandwidth varies. The above-mentioned experimental results further validate the effectiveness and enhancement of the proposed methods for system stability.

VI. Conclusion

In this article, the impact of PLL is analyzed through the MIMO impedance model of the DFIG system. It is found that the frequency-coupling phenomena are mainly caused by the transfer function matrix linked to the rotor current dynamic.

Thus, in order to eliminate the influence of the rotor current dynamic caused by PLL and improve the system stability, a second-order impedance reshaping method based on compensating the rotor current dynamic is proposed, which can eliminate the frequency-coupling effect under various operation conditions. Moreover, the negative-resistance region caused by PLL was removed, and thus, the system stability was improved a lot. Furthermore, a first-order compensation method is proposed based on simplifying the second-order reshaping method, which can also effectively suppress the oscillations, and can be easily implemented. Next, robust analysis is given to illustrate that both the proposed methods can improve the stability margin of the system when the system operating conditions and parameters vary. Finally, a control-hardware-in-loop experiment is also carried out, and the results verified the effectiveness of the theoretical analysis and the improvement for system stability of the proposed methods.

REFERENCES

[1] H. Polinder, J. A. Ferreira, B. B. Jensen, A. B. Abrahamsen, K. Atallah, and R. A. McMahon, "Trends in wind turbine generator systems," *IEEE J. Emerg. Sel. Topics Power Electron.*, vol. 1, no. 3, pp. 174–185, Sep. 2013.

[2] R. Cardenas, R. Pena, S. Alepuz, and G. Asher, "Overview of control systems for the operation of DFIGs in wind energy applications," *IEEE Trans. Ind. Electron.*, vol. 60, no. 7, pp. 2776–2798, Jul. 2013.

[3] Y. Song and F. Blaabjerg, "Analysis of middle frequency resonance in DFIG system considering phase locked loop," *IEEE Trans. Power Electron.*, vol. 33, no. 1, pp. 343–356, Jan. 2018.

[4] C. Zhang, X. Cai, M. Molinas, and A. Rygg, "On the impedance modeling and equivalence of AC/DC side stability analysis of a grid-tied Type IV wind turbine system," *IEEE Trans. Energy Convers.*, vol. 34, no. 2, pp. 1000–1009, Jun. 2019.

[5] H. Zhang, X. Wang, L. Harnefors, H. Gong, J.-P. Hasler, and H.-P. Nee, "SISO transfer functions for stability analysis of grid-connected voltage-source converters," *IEEE Trans. Ind. Appl.*, vol. 55, no. 3, pp. 2931–2941, May/Jun. 2019.

[6] Y. Xu, H. Nian, T. Wang, L. Chen, and T. Zheng, "Frequency coupling characteristic modeling and stability analysis of doubly fed induction generator," *IEEE Trans. Energy Convers.*, vol. 33, no. 3, pp. 1475–1486, Sep. 2018.

[7] Y. Sun, X. Zhang, M. Han, F. Xiao, J. Yu, and H. Zhang, "General impedance model of DFIG for wide-range-frequency oscillation studies," in *Proc. IEEE 9th Int. Power Electron. Motion Control Conf.*, 2020, pp. 2882–2886.

[8] B. Wen, D. Boroyevich, R. Burgos, P. Mattavelli, and Z. Shen, "Analysis of D-Q small-signal impedance of grid-tied inverters," *IEEE Trans. Power Electron.*, vol. 31, no. 1, pp. 675–687, Jan. 2016.

[9] B. Hu, H. Nian, M. Li, Y. Liao, J. Yang, and H. Tong, "Impedance characteristic analysis and stability improvement method for DFIG system within PLL bandwidth based on different reference frames," *IEEE Trans. Ind. Electron.*, vol. 70, no. 1, pp. 532–543, Jan. 2023.

[10] L. Fan and Z. Miao, "Mitigating SSR using DFIG-based wind generation," *IEEE Trans. Sustain. Energy*, vol. 3, no. 3, pp. 349–358, Jul. 2012.

[11] A. E. Leon, "Integration of DFIG-based wind farms into series-compensated transmission systems," *IEEE Trans. Sustain. Energy*, vol. 7, no. 2, pp. 451–460, Apr. 2016.

[12] I. Vieto and J. Sun, "Refined small-signal sequence impedance models of type-III wind turbines," in *Proc. IEEE Energy Convers. Expo.*, 2018, pp. 2242–2249.

[13] X. Wang, Y. W. Li, F. Blaabjerg, and P. C. Loh, "Virtual-impedance-based control for voltage-source and current-source converters," *IEEE Trans. Power Electron.*, vol. 30, no. 12, pp. 7019–7037, Dec. 2015.

[14] S. Xu, X. Wu, W. Gu, L. Fan, Y. Lu, and Z. Zou, "Mitigating subsynchronous oscillation using adaptive virtual impedance controller in DFIG wind farms," in *Proc. IEEE Sustain. Power Energy Conf.*, 2021, pp. 1801–1807.

[15] B. Hu, H. Nian, J. Yang, M. Li, and Y. Xu, "High-frequency resonance analysis and reshaping control strategy of DFIG system based on DPC," *IEEE Trans. Power Electron.*, vol. 36, no. 7, pp. 7810–7819, Jul. 2021.

[16] H. Tong, H. Nian, B. Hu, M. Li, H. Zhang, and Q. Liu, "High-frequency resonance analysis between DFIG based wind farm with direct power control and VSC-HVDC," in *Proc. 24th Int. Conf. Elect. Mach. Syst.*, 2021, pp. 2207–2212.

[17] D. Yang, X. Wang, F. Liu, K. Xin, Y. Liu, and F. Blaabjerg, "Symmetrical PLL for SISO impedance modeling and enhanced stability in weak grids," *IEEE Trans. Power Electron.*, vol. 35, no. 2, pp. 1473–1483, Feb. 2020.

[18] C. Wu, B. Hu, P. Cheng, H. Nian, and F. Blaabjerg, "Eliminating frequency coupling of DFIG system using a complex vector PLL," in *Proc. IEEE Appl. Power Electron. Conf. Expo.*, 2020, pp. 3262–3266.

[19] H. Nian, B. Hu, Y. Xu, C. Wu, L. Chen, and F. Blaabjerg, "Analysis and reshaping on impedance characteristic of DFIG system based on symmetrical PLL," *IEEE Trans. Power Electron.*, vol. 35, no. 11, pp. 11720–11730, Nov. 2020.

[20] Y. Zhang, C. Klabunde, and M. Wolter, "Frequency-coupled impedance modeling and resonance analysis of DFIG-based offshore wind farm with HVDC connection," *IEEE Access*, vol. 8, pp. 147880–147894, 2020.

[21] X. Zhang, Y. Zhang, R. Fang, and D. Xu, "Impedance modeling and SSR analysis of DFIG using complex vector theory," *IEEE Access*, vol. 7, pp. 155860–155870, 2019.

[22] X. Wang, L. Harnefors, and F. Blaabjerg, "Unified impedance model of grid-connected voltage-source converters," *IEEE Trans. Power Electron.*, vol. 33, no. 2, pp. 1775–1787, Feb. 2018.

[23] D. Zhu, X. Guo, B. Tang, J. Hu, X. Zou, and Y. Kang, "Feedforward frequency deviation control in PLL for fast inertial response of DFIG-based wind turbines," *IEEE Trans. Power Electron.*, vol. 39, no. 1, pp. 664–676, Jan. 2024, doi: 10.1109/TPEL.2023.3319134.

[24] D. Yang, X. Wang, F. Liu, K. Xin, Y. Liu, and F. Blaabjerg, "Adaptive reactive power control of PV power plants for improved power transfer capability under ultra-weak grid conditions," *IEEE Trans. Smart Grid*, vol. 10, no. 2, pp. 1269–1279, Mar. 2019.

[25] B. Hu, H. Nian, M. Li, Y. Xu, Y. Liao, and J. Yang, "Impedance-based analysis and stability improvement of DFIG system within PLL bandwidth," *IEEE Trans. Ind. Electron.*, vol. 69, no. 6, pp. 5803–5814, Jun. 2022.

[26] B. Liang, J. He, Y. W. Li, P. Guo, and C. Wang, "Aggregated-impedance-based stability analysis for a parallel-converter system considering the coupling effect of voltage feedforward control and reactive power injection," *IEEE Trans. Power Electron.*, vol. 36, no. 5, pp. 5954–5970, May 2021.

[27] A. J. Agbemuko, J. L. Domínguez-García, O. Gomis-Bellmunt, and L. Harnefors, "Passivity-based analysis and performance enhancement of a vector controlled VSC connected to a weak AC grid," *IEEE Trans. Power Del.*, vol. 36, no. 1, pp. 156–167, Feb. 2021.

[28] L. Huang, C. Wu, D. Zhou, and F. Blaabjerg, "Comparison of DC-link voltage control schemes on grid-side and machine-side for type-4 wind generation system under weak grid," in *Proc. 47th Annu. Conf. IEEE Ind. Electron. Soc.*, 2021, pp. 1–6.

[29] L. Huang, C. Wu, D. Zhou, and F. Blaabjerg, "A simplified SISO small-signal model for analyzing instability mechanism of grid-forming inverter under stronger grid," in *Proc. IEEE 22nd Workshop Control Model. Power Electron.*, 2021, pp. 1–6.

[30] C. Zhang, X. Cai, A. Rygg, and M. Molinas, "Sequence domain SISO equivalent models of a grid-tied voltage source converter system for small-signal stability analysis," *IEEE Trans. Energy Convers.*, vol. 33, no. 2, pp. 741–749, Jun. 2018.

Xiaoling Xiong (Member, IEEE) received the B.S., M.S., and Ph.D. degrees in electrical engineering from the Nanjing University of Aeronautics and Astronautics, Nanjing, China, in 2007, 2010, and 2015, respectively.

From 2011 to 2012, she was a Research Assistant with the Department of Electronic and Information Engineering, Hong Kong Polytechnic University, Hong Kong. Since 2015, she has been with North China Electric Power University, Beijing, China, where she is currently an Associate Professor. Simultaneously, she has been with Aalborg University, Aalborg, Denmark, where she was a Visiting Postdoctoral with the Department of Energy Technology from 2018 to 2020. Her current research interests include HVdc system, modeling, analysis, and design power electronic systems, and the study of the nonlinear behaviors in power electronic circuits.

Bochen Luo was born in Hunan, China. He received the B.S. degree in electrical engineering from the Changsha University of Science and Technology, Changsha, China, in 2021. He is currently working toward the M.S. degree majoring in electrical engineering with the School of Electrical and Electronic Engineering, North China Electric Power University, Beijing, China.

His research interests include modeling, analysis, and design of converter-based power systems.

Longcan Li received the B.S. degree in electrical engineering and its automation from the Tianjin University of Technology, Tianjin, China, in 2022. She is currently working toward the M.S. degree majoring in electrical engineering with the School of Electrical and Electronic Engineering, North China Electric Power University, Beijing, China.

Her research interests include modeling, analysis, and design of grid-following converters.

Ziming Sun (Member, IEEE) received the B.S. degree in electrical engineering in 2021 from North China Electric Power University, Beijing, China, where he is currently working toward the M.S. degree majoring in electrical engineering with the School of Electrical and Electronic Engineering.

His research interests include modeling and analysis of multiconverter distribution systems.

Frede Blaabjerg (Fellow, IEEE) received the Ph.D. degree in electrical engineering from Aalborg University, Aalborg, Denmark, in 1995, and the honoris causa from University Politehnica Timisoara, Timisoara, Romania, in 2017, and Tallinn Technical University, Tallinn, Estonia, in 2018.

He was with ABB-Scandia, Randers, Denmark, from 1987 to 1988. He became an Assistant Professor in 1992, an Associate Professor in 1996, and a Full Professor of Power Electronics and Drives in 1998 with AAU Energy. Since 2017, he has been a Villum Investigator. He has authored or coauthored more than 600 journal papers in the fields of power electronics and its applications. He is the coauthor of 8 monographs and the editor of 14 books on power electronics and its applications, e.g., the series (4 volumes): *Control of Power Electronic Converters and Systems* (Academic Press/Elsevier). His current research interests include power electronics and its applications, such as in wind turbines, PV systems, reliability, Power-2-X, power quality, and adjustable speed drives.

Dr. Blaabjerg is a recipient of 38 IEEE Prize Paper Awards, IEEE PELS Distinguished Service Award in 2009, the EPE-PEMC Council Award in 2010, IEEE William E. Newell Power Electronics Award in 2014, the Villum Kann Rasmussen Research Award in 2014, the Global Energy Prize in 2019, and the 2020 IEEE Edison Medal. He was the Editor-in-Chief of IEEE TRANSACTIONS ON POWER ELECTRONICS from 2006 to 2012. He was a Distinguished Lecturer for IEEE Power Electronics Society from 2005 to 2007 and for IEEE Industry Applications Society from 2010 to 2011 as well as 2017 to 2018. During 2019–2020, he was the President of IEEE Power Electronics Society. He is the Vice-President of the Danish Academy of Technical Sciences. From 2014 to 2021, he is nominated by Thomson Reuters to be among the most 250 cited researchers in engineering in the world.